Manuscript (word or pdf w/ figures)

This version of the article has been accepted for publication after peer review and is subject to Elsevier's terms of use, but is not the Version of Record and does not reflect post-acceptance improvements, or any corrections. The Version of Record is available online at: https://www.sciencedirect.com/science/article/abs/pii/S1359645423004998

Submitted to Acta Materialia in March 2023

Time resolved insights into abnormal grain growth by in situ synchrotron measurements

M. Vollmer[1*], S. Degener[1,2], A. Bolender[1], A. Bauer[1], A. Liehr[1], A.Stark[2], N. Schell[2], P. Barriobero-Vila[3], G. Requena[4,5], T. Niendorf[1]

[1] Universität Kassel, Institute of Materials Engineering, 34125 Kassel, Germany
[2] Helmholtz-Zentrum Hereon, 21502 Geesthacht, Germany
[3] Technical University of Catalonia (UPC), Department of Materials Science and Engineering, 08019 Barcelona, Spain
[4] German Aerospace Centre, Institute for Materials Research, 51147 Cologne, Germany
[5] RWTH Aachen University, Metallic Structures and Materials Systems for Aerospace Engineering, 52062 Aachen, Germany

Abstract

Large oligo-crystalline or single-crystalline metallic materials are of great interest for numerous applications, and a recently developed strategy for promoting abnormal grain growth induced by a cyclic heat treatment opens up new opportunities to manufacture single crystals with a size of several centimeters. So far, the entire available knowledge on this kind of abnormal grain growth has been elaborated based on time discrete observations and, thus, detailed insights into the interplay of elementary mechanisms are still lacking in open literature. The present study reveals time resolved insights into this kind of abnormal grain growth for the first time. It was possible to break down the influence of the individual heat treatment phases by *in situ* synchrotron high energy X-ray diffraction analysis during cyclic heat treatment. The results obtained not only help to gain a deep understanding of the abnormal grain growth mechanisms, they will also be the basis for an adjustment of the cyclic heat treatment process to improve the efficiency and eventually obtain even larger grains.

Keywords: single crystals, grain growth method, synchrotron diffraction, high-energy X-ray diffraction, grain boundary migration

*Corresponding Author: vollmer@uni-kassel.de

1. Introduction

Grain size influences manifold properties of metallic materials, such as mechanical, electrical or magnetic properties, and the adjustment of grain size is usually obtained by thermo-mechanical or thermal processes [1]. While small grains are preferred for the majority of applications, for specific applications such as wavers or turbine blades, oligo-crystalline or even single-crystalline states are of great interest [2–7]. However, such large grains can hardly be obtained by normal grain growth. Therefore, complex and cost-intensive techniques such as Bridgman-Stockbarger [8,9] or Czochralski [10] are often used.

Under specific circumstances it is also possible that one or a few grains grow rapidly in a polycrystalline material and thereby consume the neighboring grains [1,11–15]. This process is known as abnormal grain growth (AGG) and can lead to grains of several millimeters in size. Such evolution only occurs, if abnormally growing grains gain energetic advantages over the engulfed grains. Well-known factors promoting AGG are the free surface energy, texture, second phase precipitates as well as dislocation density differences between neighboring grains [1,12].

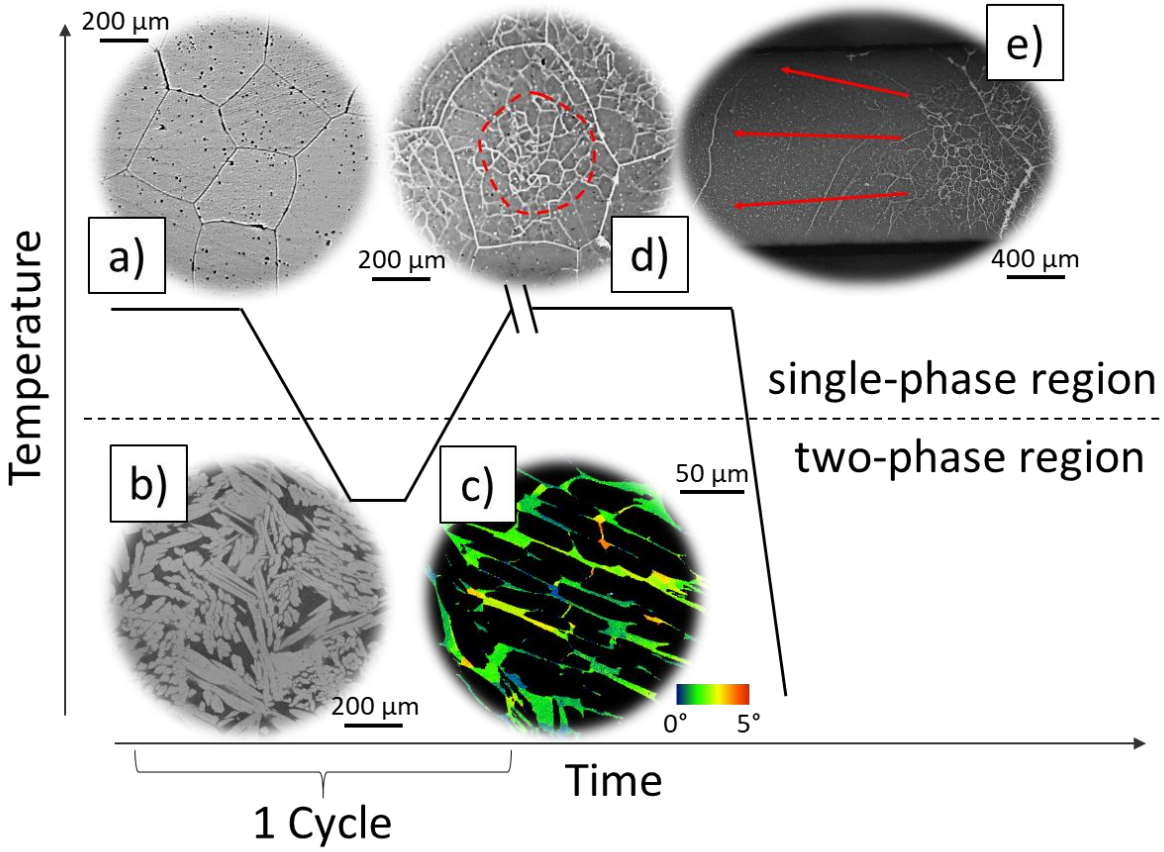

Figure 1: Schematic detailing the time-temperature curve to be passed during an AGG heat treatment cycle. The characteristic microstructure images show (a) the grains after initial annealing in the single-phase region, (b) the microstructure in the two-phase region, (c) a grain reference orientation deviation map of the parent phase, (d) subgrains after dissolution of the second phase (the area with a higher density of subgrains in the interior of the grain is highlighted by the red dashed circle) and (e) an abnormal grown grain [16].

In 1988 a novel kind of AGG was discovered [17–19] and later systematically studied by Omori et al. [20]. The abnormal grown grains were observed as a result of a cyclic heat treatment (CHT) between a high-temperature single-phase region and a low-temperature two-phase region (cf. Fig 1). It was shown that subgrain structures were present in the high-temperature phase after

passing through the two-phase region, and it was supposed that the corresponding subgrain boundaries provide the necessary energetic advantages for some specific grains to grow at the expense of their neighbors. In particular, it was assumed that the coherency-loss during growth of the second phase leads to a high dislocation density in the parent phase and subsequently to the formation of subgrains during second phase dissolution. These subgrains are unequally distributed within the grains, i.e. the density of subgrains is lower in the direct vicinity of high-angle grain boundaries and higher in the grain interior (cf. Fig 1d). In a subsequent step, the grains start to grow normally and those grains which first overcome the low-density subgrain zones of their neighbors are supposed to grow abnormally [21].

The additional Gibbs energy $\Delta G_{s,}$ provided by the subgrains, can be calculated by the following equation [14,22,23]:

$$\Delta G_s = \frac{c_s \gamma_s V}{r_s} \quad (1)$$

where γ_s is the subgrain boundary surface energy, r_s is the mean grain radius of the subgrains, V is the molar volume of the single-phase and c_s is a growth mode dependent constant.

From equation (1) it is obvious that the Gibbs energy can be increased either by a higher misorientation, which correlates with a higher subgrain boundary surface energy γ_s, or by a smaller radius of the subgrains r_s. Both factors were shown to have a positive impact on the grain growth rate in recent studies [21,24,25]. Since the heat treatment cycles can be repeated for several times, it is possible to promote the evolution of large single crystals with a size of more than 20 cm [21,24]. Moreover, recently a massive reorientation of such single crystals by further CHTs was observed. Such effect can be exploited to adjust beneficial orientations [26]. As an example, such specific material conditions are promising for applications as dampers as well as self-centering or prestressing elements in civil engineering [27–29].

Up to now, investigations of this kind of AGG were only based on time-discrete information, i.e. specimens were quenched at certain points of the heat treatment and subsequently investigated at room temperature. However, investigations of the dynamic processes within the material during the CHT are not available in open literature. Thus, the present study was conducted to provide time-resolved insights into the mechanisms of this kind of AGG for the first time. A Fe-Mn-Al-Ni-Ti alloy, where a high driving force for AGG was demonstrated in previous studies [24,30], was used as test material. The alloy is characterized by a body-centered cubic α phase in the single-phase region at high temperatures, which is referred to as parent phase in the remainder of the text, and a mixture of α phase and face-centered cubic γ phase in the two-phase region [31]. The γ phase is referred to as second phase in the remainder of the text. Moreover, a minor fraction of an ordered body-centered cubic β precipitates prevails in the initial condition of the alloy (cf. Fig. 2a), which is known to highly affect the resulting mechanical properties of the alloy system [29,32–35]. However, the β precipitates disappear upon initial heating. It is important to note that the formation of the precipitates only starts at much lower temperatures compared to the temperatures applied during CHT [36]. Thus, an influence of the precipitates on AGG can be excluded and will not be in focus in the remainder of the study.

A specimen was investigated by means of synchrotron high energy X-ray diffraction (HEXRD) at the High Energy Materials Science (HEMS) beamline P07 (PETRA III, DESY, Hamburg [37]) and subjected to a CHT, which was applied by a modified Bähr DIL 805 A/D dilatometer [38]. Moreover, additional measurements of specimens, where the CHT was interrupted by quenching, were made by means of synchrotron HEXRD, optical microscopy (OM) and electron backscatter diffraction (EBSD) to support the findings of the *in situ* measurement.

2. Methods

The investigated specimens were wire-cut by electrical discharge machining from a Fe-34.0Mn-15.0Al-7.5Ni-1.5Ti (at. %) ingot, which was produced by vacuum induction melting. Specimens with a diameter of 4.5 mm and a length of 10 mm were investigated by means of synchrotron HEXRD diffraction. Before thermal treatments were conducted, the surface was ground down to 5 µm grit size and subsequently polished with 3 µm and 1 µm diamond suspension, respectively. Afterwards, one specimen was equipped with a thermocouple for temperature measurement and mounted inside the modified dilatometer of the synchrotron HEXRD facility. The CHT started with a heating from RT to 1175°C with a rate of 2.5 K s^{-1}. Afterwards, the specimen was held for a dwell time of 3 minutes at 1175°C, cooled down to 800°C with a rate of 10 K min^{-1} and held in the two-phase region for 3 minutes. Subsequently, the specimen was heated up again to 1175°C with a rate of 10 K min^{-1}, and after a dwell time of 10 minutes, the specimen was quenched to room temperature.

During the CHT the diffraction patterns were collected with 0.1 s acquisition time. Ten images were summed, finally resulting in 5723 images and an acquisition rate of 1 Hz. The diffraction measurements were performed using a Perkin Elmer XRD1621 area detector with 2048 pixels × 2048 pixels and a pixel size of 200 µm. The specimen-detector distance was 746 mm. With a synchrotron radiation energy of 99.98726 keV and a primary beam size of 0.8 mm × 0.8 mm more than ten diffraction peaks of the parent phase were present.

The setup calibration was done using the Python module PyFAI [39,40] with diffraction data of a LaB6 standard powder specimen. For the characterization of the phase evolution the diffraction images were fully integrated in Python using PyFAI. The resulting diffractograms

were analyzed in MATLAB to detect the diffraction peaks present and, by this, to determine the present phases and their varying lattice parameters.

The initial grain distribution was described by orientation distribution functions (ODF) calculated from pole figure data using the MATLAB package MTEX [41]. Pole figure data were derived from cake-integrated diffraction patterns with an azimuthal resolution of 1° based on the method of Wenk and Grigull [42]. For the coarse-grained diffraction patterns with only discrete diffraction spots, pole figure data were also generated, followed by an analysis to determine single orientations considering the specific location and number of recorded diffraction spots in MATLAB.

For a qualitative investigation of the evolution of number of grains, the diffraction spots of each lattice plane for the entire azimuthal range were extracted by the function “find_peaks” of the Python module “scipy.signal” and summed up for better statistics [43]. Based on such approach, scattering due to the varying number of diffraction spots for each lattice plane and for different grain orientations can be reduced.

Furthermore, diffraction poles of grains showing AGG and engulfed grains were extracted and selected to determine their azimuthal pole width as full width at half maximum (FWHM) over the CHT by fitting a Gaussian function. A nonlinear curve-fitting (least-squares sense solver, lsqcurvefit) was applied to these poles in MATLAB.

To characterize the grain size and grain orientations after the *in situ* experiment, the specimen in focus was cut parallel to the beam direction, ground down to 5 µm grit size and vibro-polished using a colloidal SiO_2 suspension with 0.02 µm particle size. EBSD measurements were conducted using a Zeiss Ultra SEM operated at 20 kV equipped with an EBSD detector. For OM the specimen was etched with a solution of 3% nitric acid and 97% ethanol.

To investigate the influence of subgrains on the FWHM values of poles, two specimens were heat treated as follows: The first specimen was solution treated at 1225°C for 60 min and subsequently water quenched. The second specimen was first solution treated at 1225°C for 30 min, afterwards cooled down to 900°C with a rate of 10 K min^{-1}, held for 15 min and subsequently again heated up to 1050°C with a rate of 10 K min^{-1}, before directly being subjected to water quenching. Afterwards, ex situ synchrotron HEXRD measurements were conducted with the same setup as for the *in situ* measurement. To ensure that the solution treated and subsequently quenched specimen was free of subgrains and that the second specimen possesses a high number of subgrains, respectively, both specimens were also cut parallel to the beam direction, ground down to 5 µm grit size and vibro-polished using a colloidal SiO_2 suspension with 0.02 µm particle size. Afterwards, the presence of subgrains was checked by means of color orientation contrast imaging (COCI) [44] using the above mentioned Zeiss Ultra SEM operated at 20 kV equipped with an EBSD detector with a forescattered electron (FSE) imaging system.

Two specimens with a cross-section of 1.5 mm × 1.6 mm and a gauge length of 18 mm were used to investigate the misorientation of subgrains in the two-phase region as well after dissolution of the second phase. Specimens were ground down to 5 µm grit size before being heat treated. The first specimen was solution-treated at 1225°C for 30 min, cooled down with a rate of 10 K min^{-1} into the two-phase region at 900°C and water quenched after a dwell-time of 15 min. The second specimen was also solution treated at 1225°C for 30 min, cooled down with a rate of 10 K min^{-1} into the two-phase region at 900°C and heated up with a rate of 10 K min^{-1} to 1050°C after a dwell time of 15 min. Subsequently, the specimen was immediately water quenched. Both specimens were again prepared by grinding and vibro-polishing following the above-mentioned procedures. Afterwards, the same SEM/EBSD system was used for

misorientation measurements. The distributions of the grain reference orientation deviations (GROD) were afterwards extracted from the EBSD measurements.

To show the subgrain morphology slightly after beginning of AGG, a Fe-Mn-Al-Ni specimen with a chemical composition of Fe-34.0Mn-15.0Al-7.5Ni (at%) was used instead of a Fe-Mn-Al-Ni-Ti specimen. This is justified by the much lower grain growth velocity (cf. [24]) and the better chance to see grains in the initial stage of AGG. The cross-section was 1.5 mm × 1.6 mm and the gauge length 18 mm. After the specimen was ground down to 5 µm grit size, it was solution treated at 1225°C for 30 min, afterwards cooled down with a rate of 10 K min^{-1} to 900°C, held for 15 min and subsequently heated up with a rate of 10 K min^{-1} to 1225°C again, directly followed by water quenching. Afterwards, it was again ground down and vibro-polished as detailed before. For OM the specimen was etched with the solution of 3% nitric acid and 97% ethanol. All investigated specimens and the corresponding testing methods are summarized in Table 1.

Table 1: Summary of the tested specimens and corresponding investigations

Specimen	Alloy	Heat treatment	Investigations				
			in situ HEXRD	ex situ HEXRD	OM	EBSD	COCl
1	Fe-Mn-Al-Ni-Ti	A	x		x	x	
2	Fe-Mn-Al-Ni-Ti	B		x			x
3	Fe-Mn-Al-Ni-Ti	C		x			x
4	Fe-Mn-Al-Ni-Ti	C				x	
5	Fe-Mn-Al-Ni-Ti	D				x	
6	Fe-Mn-Al-Ni	E			x		

A: 2.5 K min^{-1} --> 1175°C 3 min --> 10 K min^{-1} --> 800°C 3 min --> 10 K min^{-1} --> 1175°C 10 min --> quenched

B: 1225°C 60 min --> water quenched

C: 1225°C 30 min --> 10 K min^{-1} --> 900°C 15 min ---> 10 K min^{-1} --> 1050°C 0 min --> water quenched

D: 1225°C 30 min --> 10 K min^{-1} --> 900°C 15 min --> water quenched

E: 1225°C 30 min --> 10 K min^{-1} --> 900°C 15 min ---> 10 Kmin^{-1} --> 1225°C 0 min --> water quenched

3. Results

Phase evolution

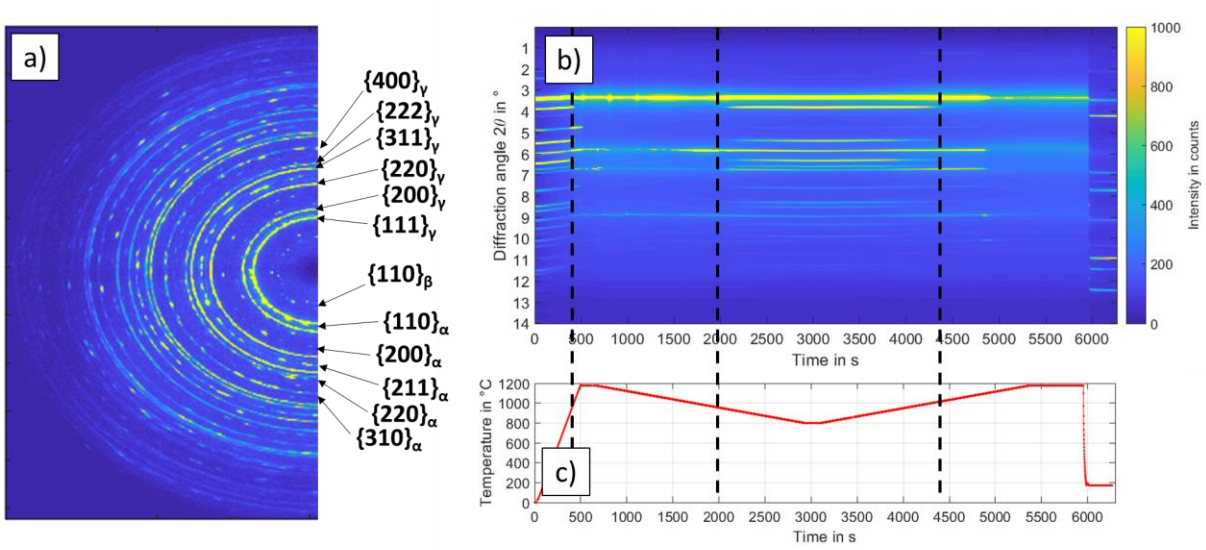

Figure 2: Investigation of the phase evolution during the CHT. (a) Characteristic synchrotron diffraction pattern from the beginning of the experiment (at room temperature) with indexed phases. (b) Summed intensities of the different diffraction angles over time. (c) Time-temperature curve of the CHT. The dashed lines highlight the points, where the second phase occurs and disappears.

Figure 2a shows a synchrotron diffraction pattern from the initial state of the experiment at room temperature. Each diffraction ring can be indexed by a certain phase and set of equivalent planes of the investigated material, as it is exemplary highlighted in the right part of the image. To evaluate the evolution of phases over time, the intensities of each ring were summed for each diffraction pattern image. The summed intensities of the different rings, represented by the different diffraction angles 2θ, over time are shown in Fig. 2b. It is obvious that some diffraction

angles offer considerable intensities during the whole experiment, whereas others disappear or arise over time. Moreover, especially at the beginning of the heating cycle and during quenching at the end of the experiment minor shifts of intensity lines are seen. These can be attributed to changes of lattice parameters due to thermal expansion and shrinkage, respectively. By direct correlation of the diffraction angles and the involved phases, as well as the time and the temperature profile, which was directly measured at the specimen surface, it is possible to determine the temperatures, where the different phases form and dissolve.

Upon initial heating, the above mentioned β phase as well as the second phase disappear at temperatures of about 950 °C (380 s) and 1025°C (410 s), respectively. Thus, during the first solution annealing at 1175°C only the parent phase is present. During subsequent cooling the second phase evolves again at about 951°C (1994 s) and dissolves during heating at about 1015°C (4370 s). Afterwards, some intensity lines at diffraction angles corresponding to the parent phase disappear. This disappearance provides a first evidence of AGG activities, since these intensity lines disappear as a result of a lower number of grains being probed by the beam. The remaining grains furthermore are unfavorably oriented with respect to the diffraction angles. After quenching, some additional intensity lines related to diffraction angles belonging to the parent phase occur. This effect can be attributed to a slight tilt or contraction of the specimen and the crystal lattice during quenching. Such change slightly influences the lattice plane diffraction angles and, thus, the scattering vectors. Moreover, it leads to a variation of grain orientations being in diffraction condition and, therefore, contributing to the recorded diffraction patterns.

Subgrain evolution

It is assumed that the formation and subsequent dissolution of the second phase leads to the formation of dislocation structures and eventually to the occurrence of subgrain structures, which in turn provide the necessary energy for some grains to grow abnormally.

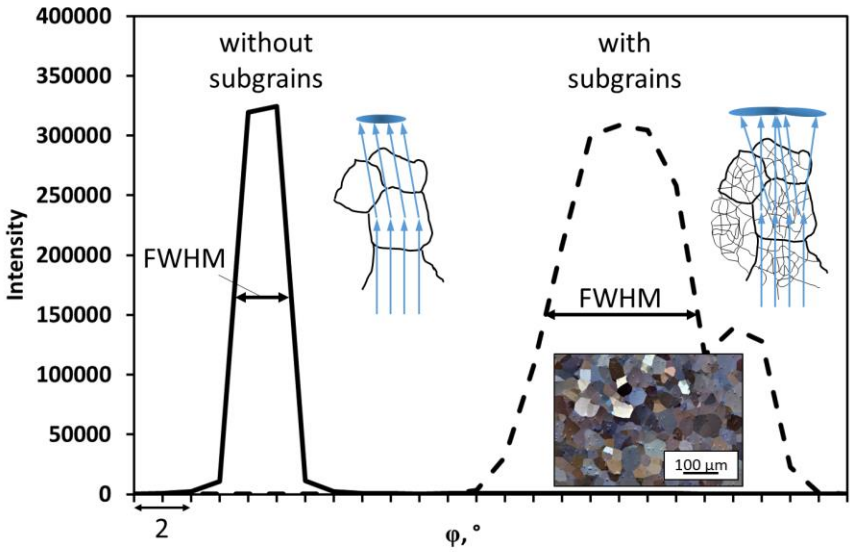

Figure 3: Characteristic diffraction poles of the {220}$_\alpha$ planes of a specimen being solution annealed and subsequently quenched (without subgrains) and of a specimen that was quenched in the second half of the CHT immediately after the second phase was dissolved (with subgrains). The inset shows a COCI of the subgrains. Schematics highlight how the subgrains influence the HEXRD.

To determine the fraction of subgrain structures during the CHT, FWHM values were evaluated for different poles of the diffraction pattern. It is important to note that the pole width, i.e. the intensity expansion of the pole along the ring azimuth, is dominated by the distribution

of the misorientations being present within a grain, resulting in a wider fulfilment of the diffraction condition regarding the φ angle. In contrast, the peak width, i.e. the radial expansion of the pole, is a convolution of the Bragg peak influenced by the presence of micro strains, dislocations, grain size, temperature effects and the misorientation within the grain, which in summary is leading to deviations of 2θ [45–48]. Figure 3 shows a characteristic diffraction pole of the $\{220\}_{\alpha}$ planes of a specimen that was solution annealed and subsequently quenched, i.e. a specimen without subgrains (cf. Fig. 1a). In direct comparison, a characteristic diffraction pole of the $\{220\}_{\alpha}$ planes of a specimen being quenched in the second half of the heat treatment cycle immediately after the second phase was dissolved, i.e. a specimen with a high fraction of subgrains (cf. Fig. 1d), is shown. It is obvious from the diffraction poles in Fig. 3 that the FWHM values of the pole width differ significantly between both conditions, i.e. by a factor of about 2.5, whereas the peak width is almost equal in both conditions (not shown) supporting the good correlation between FWHM values of the pole width and misorientation. Furthermore, it is observed that the broadening of the poles in the condition with subgrains often results in a pole distribution with some additional local intensity maxima, which is also present in Fig. 3. In addition, microstructural and thermal factors can further influence the pole width. Still, tracking of the FWHM values over time seems to be reasonable to investigate the subgrain evolution during AGG qualitatively.

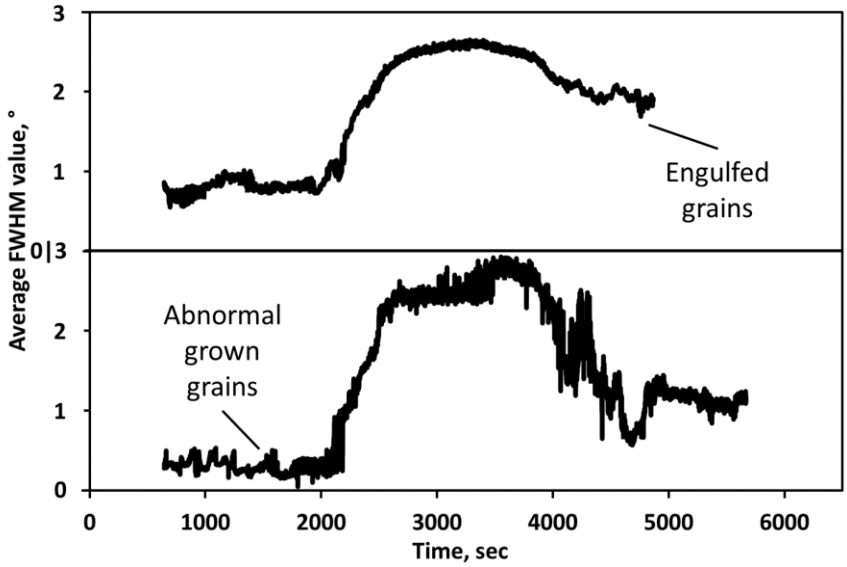

Figure 4: Plot of the average FWHM value of the pole widths over time related to four poles of grains being engulfed during AGG and three poles of grains that grew abnormally.

Figure 4 shows plots of average FWHM values over time related to four poles of grains being engulfed during AGG and three poles of grains that show AGG. It can be seen that both average FWHM values oscillate around 0.8° and 0.3°, respectively, at the beginning, start to increase after about 2000 seconds and achieve a maximum at about 3300 seconds. Afterwards, both average FWHM values decrease. However, at about 4400 seconds, the average FWHM value related to the poles of the engulfed grains remains almost constant at about 1.9°, whereas the average FWHM value related to the poles of the abnormal growing grains further decreases. After about 4900 seconds the average FWHM value related to the poles of the engulfed grains disappears. This fact again can be related to the AGG activities. The considered grains are engulfed by the abnormally growing grains and finally the corresponding grains including their poles dissolve. Using the time values listed above, it is possible to link the FWHM value evolution to the corresponding temperatures. The increasing FWHM values at about 2000

seconds correspond to a temperature of about 950°C and, thus, to the beginning of second phase formation. The peak value at about 3300 seconds corresponds to a temperature of about 830°C. Finally, the divergence of both FWHM values at about 4400 seconds is related to the complete disappearance of the second phase at about 1015°C.

Grain growth

To determine the course of grain growth over time, the poles of different rings of the parent phase, i.e. lattice planes of the parent phase, over time were evaluated. Due to its crystallographic orientation, each grain in the investigated specimen volume leads to distinctive poles in the synchrotron diffraction pattern. The more grains with different orientations are present, the more poles appear on the diffraction image. Vice versa, if the grain size becomes very large, or if all grains have the same orientation, only a few high intensity poles are observable. Although the synchrotron diffraction pattern can also change due to thermal expansion or shrinkage and due to tilting of the specimen, it is possible to detect significant changes in terms of grain size during the CHT. By summing the number of poles of five different sets of equivalent planes of each synchrotron diffraction pattern, the impact of specific orientations on the present poles and the already mentioned dynamic change of specimen conditions can be reduced effectively. Thus, it is possible to plot the number of accumulated poles over time, as it is shown in Fig. 5.

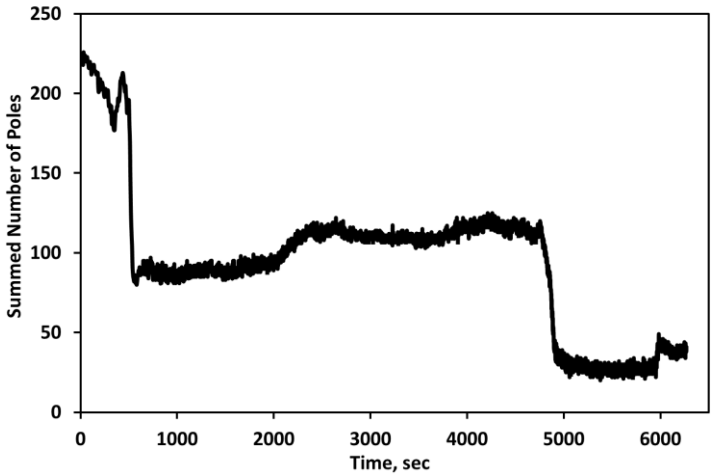

Figure 5: Summed number of poles of the $\{200\}_\alpha$, $\{211\}_\alpha$, $\{220\}_\alpha$, $\{321\}_\alpha$ and $\{411\}_\alpha$ planes over time.

It is obvious that the summed number of poles decreases rapidly (in two stages) during the CHT. The first drop occurs at about 500 seconds, which corresponds to the beginning of the dwell time at the high temperature level (i.e. 1175°C). It is likely that this drop is related to a first grain growth event. Afterwards, the summed number of poles remains nearly constant and is only slightly influenced by the occurrence and dissolution of the second phase. The second drop, which can be clearly attributed to the occurrence of AGG, takes place between 4750 and 4900 seconds, which can be related to 1074 and 1099 °C, respectively. After the second drop, the summed number of poles again remains constant. Only slight changes are observable during quenching, which are likely related to changed lattice parameters or slight orientation changes. However, these minor deviations are not in the scope of the present study.

4. Discussion

Up to here only single features of the synchrotron diffraction pattern were evaluated and related to the time and temperature history of the investigated specimen. However, to shed light on the mechanisms of AGG during CHT, the specific findings have to be related to each other.

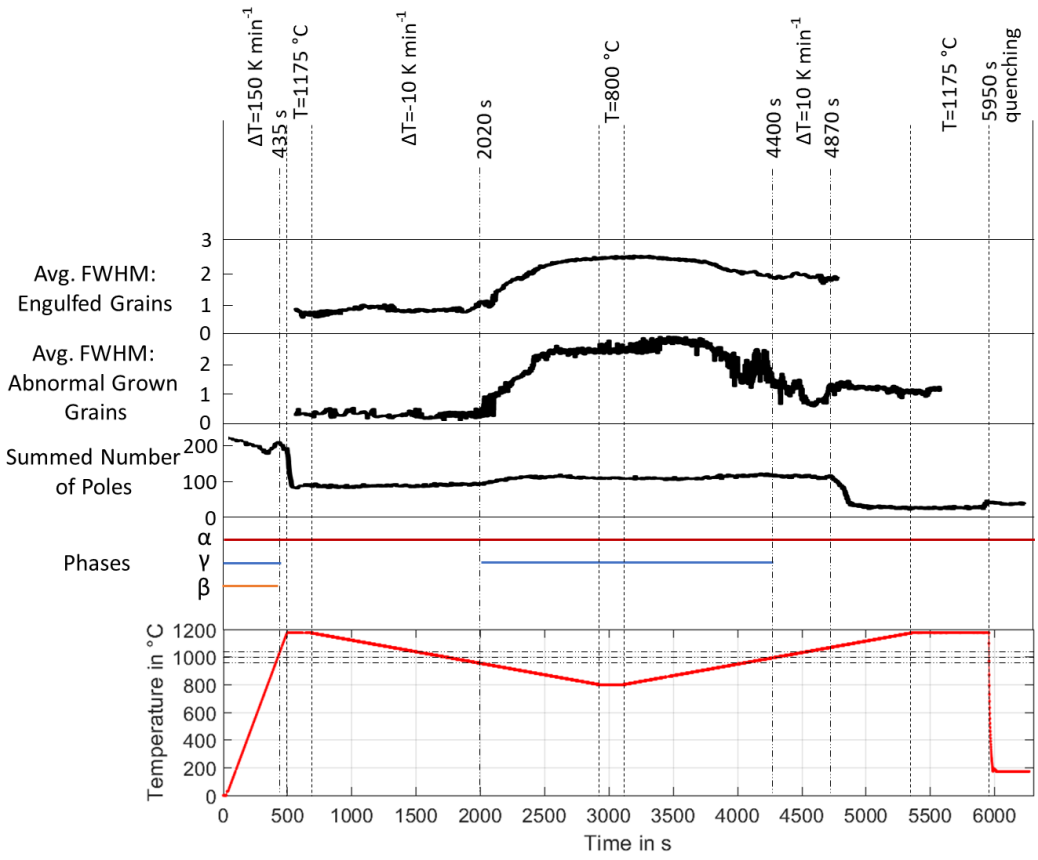

Figure 6: Phase evolution, average FWHM values related to poles of engulfed grains and of abnormal grown grains, respectively, the summed number of poles of the $\{200\}_\alpha$, $\{211\}_\alpha$, $\{220\}_\alpha$, $\{321\}_\alpha$ and $\{411\}_\alpha$ planes, as well as the measured temperature over time. Temperatures and times of specific interest are marked by dashed lines.

Figure 6 correlates the phase evolution, the average FWHM values related to the poles of engulfed grains and of abnormal grown grains, respectively, the summed number of poles of the $\{200\}_\alpha$, $\{211\}_\alpha$, $\{220\}_\alpha$, $\{321\}_\alpha$ and $\{411\}_\alpha$ planes, as well as the measured temperature over time. It is obvious that the initial heating leads to the dissolution of the β phase and the second phase (γ). Subsequently, grain growth activities can be observed as indicated by the decreasing summed number of poles. Even if the drop of the summed number of poles is relatively strong, it can be likely related to normal grain growth. Previous studies already showed a homogeneous grain size distribution without traces of subgrains after solution annealing [24]. Moreover, due to the high heating rate of 150 K min^{-1} during the initial heating, there was a high driving force for normal grain growth after dissolution of the second phase.

After the first drop of the summed number of poles, grain growth activities are hardly observable during the dwell time at 1175°C, i.e. the summed number of poles stays nearly constant. In the subsequent cooling step gamma phase occurs at around 2000 s, which can be linked to a temperature of about 950 °C. At this point the average FWHM values related to the poles of the abnormal grown grains, as well as to poles of the engulfed grains, start to increase. As already mentioned before, the formation of the semi-coherent second phase is supposed to lead to a high dislocation density in the parent phase. and in direct interplay with the relatively high temperatures, which promotes dislocation motion, it can be assumed that subgrain formation immediately begins, i.e. directly after the second phase starts to occur. These findings are in good agreement with EBSD measurements of presented in various studies [20,21,23,24], where the specimens were quenched after a given dwell time in the two-phase region eventually showing high orientation deviations in the parent phase (cf. Fig 1c).

At this point it should be noted that the FWHM values increase non-linearly with decreasing temperature, i.e. FWHM values tend to reach a maximum near the temperature plateau at about 800°C. At this temperature a maximum volume fraction of the second phase in Fe-Mn-Al-Ni-Ti can be obtained, as previous studies already revealed [24]. It is reasonable that the volume fraction of the semi-coherent second phase is directly linked to the FWHM values and, thus, to the formation and misorientation of subgrains. Consequently, an increasing amount of second phase leads to higher misorientations of the subgrains within the parent phase. After the maximum of the volume fraction of the second phase is reached, no further changes are observable. Following the given dwell time at 800°C, the temperature was again increased and the volume fraction of the second phase decreased, until the second phase completely disappeared at around 4400 s, i.e. at about 1015°C. During dissolution of the second phase, the FWHM values of both kinds of poles continuously decreased, which means that the dissolution of the second phase does not contribute to higher subgrain misorientations, but rather leads to a decrease of the misorientations. As can be deduced from Fig. 7a, this finding is in good agreement with grain reference orientation deviation (GROD) measurements within the parent phase conducted on a specimen that was quenched immediately after the maximum dwell time in the two-phase region and on a second specimen being quenched immediately after dissolution of the second phase.

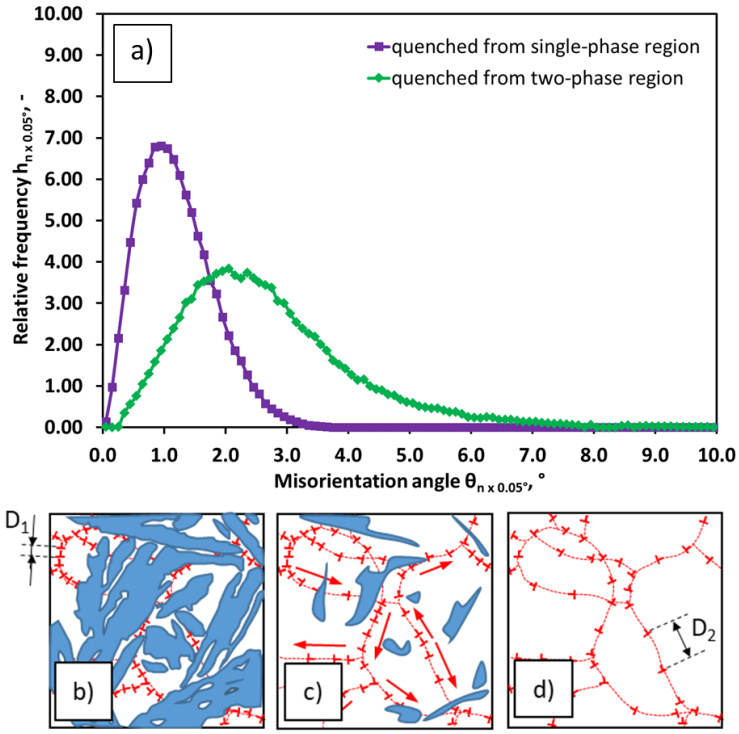

Figure 7: (a) GROD of a specimen quenched after maximum dwell time in the two-phase region (green) and quenched immediately after dissolution of the second phase (violet). Schematic highlighting the dislocation distribution and subgrain formation in the two-phase region with a high fraction of second phase (b), during partial dissolution of the second phase (c) and after complete dissolution of the second phase (d).

While the former specimen is characterized by a gaussian distribution that is broader and has its peak at a higher misorientation value of about 2°, the second specimen shows a narrower distribution with a peak at about 1° misorientation. Even if the exact mechanism of subgrain formation as a result of second phase formation and dissolution is not clear yet, some considerations can be taken into account to assess the misorientation decrease during second phase dissolution. In general, low-angle grain boundaries can be considered as an array of dislocations, and the misorientation angle θ can be described as follows [49]:

$$\theta = 2\sin^{-1}\frac{|b|}{2D} \quad (2)$$

where |b| is the absolute value of the Burgers vector, and D is the distance between two dislocations [50]. It can be assumed that the dislocation density increases during formation of the semi-coherent second phase. Then, the spacing between the dislocations is small as long as the volume fraction of the second phase is high (as it is shown in the schematic in Fig. 7b). If the temperature increases and the second phase starts to disappear, the volume fraction of the parent phase increases, and it is likely that the existing dislocations start to move, as it is indicated by the red arrows in Fig. 7c. From these considerations, it becomes obvious that the distance between the dislocations becomes larger after complete dissolution of the second phase (D_2 in Fig. 7d) and, therefore, a decrease of the misorientation angle can be observed. Such a decrease of misorientation at high temperatures by cooperative climbing of dislocations was initially proposed by Li [51].

After complete dissolution of the second phase, the average FWHM value of poles belonging to engulfed grains remains almost constant, until AGG occurs. However, the average FWHM value of these engulfed grains is higher compared to the value before second phase formation, i.e. a certain number of subgrains remains within these grains, until AGG occurs.

In contrast, the average FWHM value of poles belonging to the abnormal grown grains still decreases after second phase dissolution. In terms of misorientation, this means that the misorientation in the investigated grains further decreases, before AGG occurs. Up to now, it is assumed that all grains, i.e. the later engulfed and the abnormal grown grains, form subgrains similarly and that the selection of abnormal growing grains depends on which grain first overcomes the low density subgrain zones of its neighbors. However, the present results clearly indicate that the selection of the abnormal growing grains can be determined immediately after

second phase dissolution, i.e. by assessment of the decreasing FWHM values of such grains. This is quite unexpected, since previous studies revealed traces of subgrains in abnormally grown grains [21,24,52], i.e. subgrains remain in the area where the grain was probably located before AGG. Thus, misorientations were expected to be similar in grains which will be later engulfed and grains which will later grow abnormally.

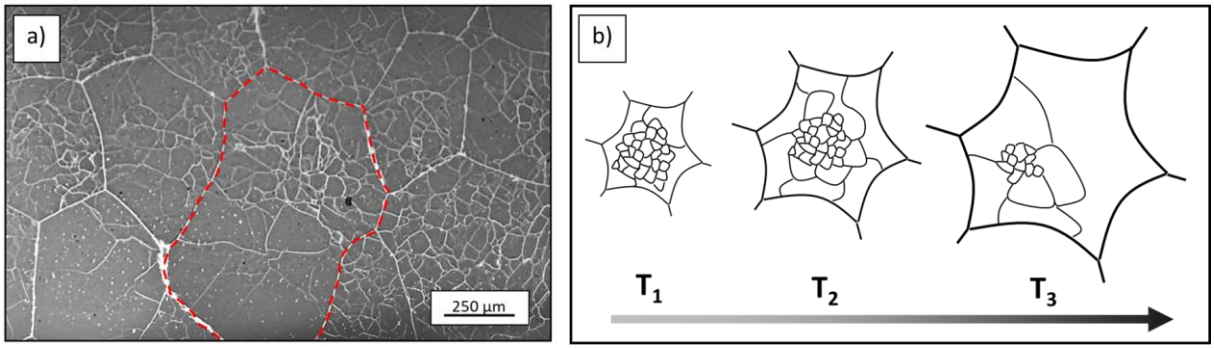

Figure 8: (a) OM image of a specimen immediately quenched after initiation of AGG with an abnormal growing grain highlighted by the red dashed line. (b) Schematic of an abnormal growing grain immediately after second phase dissolution (T_1), during the normal grain growth process (T_2) and immediately before AGG starts (T_3).

Figure 8a shows a characteristic OM image of a specimen which was immediately quenched after AGG occurred. An abnormally grown grain is highlighted by the dashed line. It can be seen that a small area in the upper part of the grain reveals subgrains with a similar size compared to the subgrains of most of the surrounding grains. In the direct vicinity of this core area the subgrains become larger, and the boundaries of the subgrains merge into the high-angle grain boundaries. An explanation for the decreasing misorientation in the grains which later grow abnormally may be that during normal grain growth the subgrain boundaries start to migrate in

direction of the high-angle grain boundaries (cf. Fig. 8b). In this case all dislocations of a subgrain boundary migrate in the same direction enabled by dislocation slip, and due to the growth of the subgrains, the distance between the dislocations increases [53]. As already mentioned before, this would lead to a decrease of misorientation of the subgrains in accordance to equation 2 and, thus, to a decrease of the FWHM value. However, it should be noted that the observation of decreasing FWHM values is only based on a few poles, since the number of grains after AGG is low. Therefore, further investigations on the role of decreasing misorientations on the selection of growing grains have to be made in future studies.

A second drop of summed number of poles can be observed between 4750 and 4900 s, i.e. between 1074 and 1099 °C. This second drop can be clearly attributed to the onset of AGG. Thereby, poles of engulfed grains disappear, and poles of the abnormal grown grains remain. Here, it is obvious that the FWHM values of the engulfed grains vanish during this time. After 4900 s, no further changes of summed number of poles are seen, i.e. the grain growth takes place in a very short time period of just 150 s. To estimate the growth rate of the grains during AGG, the investigated specimen was cut orthogonal to the beam, and OM was applied to measure the size of the abnormal grown grains. Moreover, EBSD was used to ensure that the individual grains correlate to the diffraction spots of the synchrotron diffraction pattern (not shown). The largest dimension of a grain which was hit by the beam was about 4700 µm (cf. Fig. 9). Taking into account an initial size of 400 µm after solution treatment [24] and a growth time of about 150 s, the grain growth rate can be estimated to be about 29 µm s^{-1}. This is in the same order of magnitude as previous results of Fe-Mn-Al-Ni-Ti revealed [24].

From the insights provided into the AGG mechanisms, it will be possible to tailor the CHT procedure, e.g. by accelerating or slowing down heating and cooling rates or dwell times at

specific points of the heat treatment procedure. Thereby, it will be feasible not only to shorten the time of the CHT, but also to enhance the final size of the grains established by AGG.

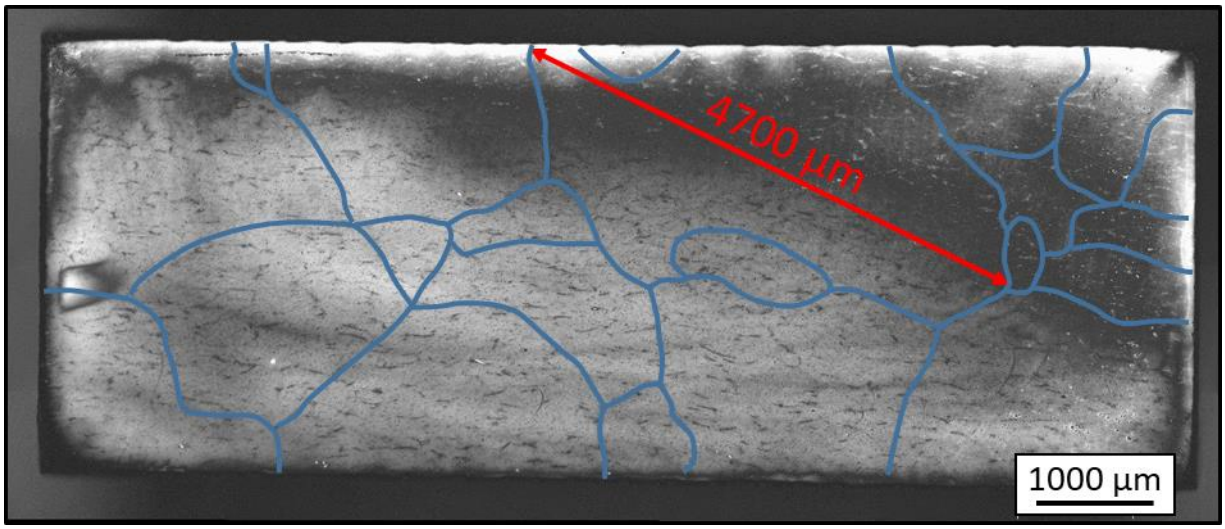

Figure 9: OM image of the specimen after in situ synchrotron HEXRD analysis revealing elementary mechanisms stimulated by CHT. Grain boundaries are marked by blue lines. The largest grain dimension is highlighted by a red double-arrow.

5. Conclusions

The present study revealed time-resolved insights into AGG induced by CHT for the first time. An *in situ* synchrotron HEXRD experiment during a specific CHT cycle in combination with *ex situ* microstructural investigations allowed for in-depth analysis of the AGG process. Thereby, not only a thorough understanding of the prevailing mechanisms was attained, the obtained insights into AGG can also be used to tailor the CHT process itself. Based on the results shown, the following conclusions can be drawn:

- The formation of subgrains, which provide the necessary energy for AGG, highly depends on the formation and dissolution of the second phase. It was shown that the subgrains already occur during formation of the second phase and that the misorientation correlates with the volume fraction of the second phase, i.e. the larger the volume fraction of second phase, the higher the misorientation. During dissolution of the second phase, the misorientation decreases probably due to an increased volume fraction of the parent phase, eventually leading to dislocation movement and, thus, to a larger distance between the dislocations.
- The results obtained indicate that the time between second phase solution and occurrence of AGG is essential for the selection of growing and engulfed grains. While the misorientation of the subgrains remains almost constant in the engulfed grains, the misorientation of the abnormal grown grains seems to further decrease, which may be related to the growth of subgrains during normal grain growth.
- The time slot, where the AGG occurs, is short in direct comparison with the entire CHT procedure. The estimated grain growth rate was 29 µm s^{-1}, this value is based on a growth distance of 4200 µm in 150 s.

Acknowledgements

Financial support by Deutsche Forschungsgemeinschaft (project number 447247560) is gratefully acknowledged. We acknowledge DESY (Hamburg, Germany), a member of the Helmholtz Association HGF, for the provision of experimental facilities. Parts of this research were carried out at PETRA III, and we would like to thank C. Sobrero, B. Aminforoughi and P. Krooß for assistance in using P07. Beamtime was allocated for proposal I-20190564. P.B.-V. acknowledges financial support from the Spanish Ministry of Science through the Ramón y Cajal grant RYC2020-029585-I.

References

[1] F.J. Humphreys, M. Hatherly, Recrystallization and related annealing phenomena, 2nd ed., Elsevier, Amsterdam, Boston, 2004.

[2] S.-E.E. Park, W. Hackenberger, Current Opinion in Solid State and Materials Science 6 (2002) 11–18.

[3] C. Ding, H. Jia, Q. Sun, Z. Yao, H. Yang, W. Liu, X. Pang et al., J. Mater. Chem. C 9 (2021) 7829–7851.

[4] Q. Ding, H. Bei, X. Zhao, Y. Gao, Z. Zhang, Crystals 10 (2020) 572.

[5] R. Fornari (Ed.), Single crystals of electronic materials: Growth and properties, Woodhead Publishing an imprint of Elsevier, Duxford, Cambridge, MA, Kidlington, 2019.

[6] S. Dost, B. Lent, Single crystal growth of semiconductors from metallic solutions, Elsevier, Amsterdam, 2007.

[7] D.-H. Neuhaus, A. Münzer, Advances in OptoElectronics 2007 (2007) 1–15.

[8] P.W. Bridgman, Proceedings of the American Academy of Arts and Sciences 60 (1925) 305.

[9] D.C. Stockbarger, Review of Scientific Instruments 7 (1936) 133–136.

[10] J. Czochralski, Zeitschrift für Physikalische Chemie 92U (1918).

[11] P.J. Noell, E.M. Taleff, JOM 67 (2015) 2642–2645.

[12] P.J. Noell, E.M. Taleff, Metall and Mat Trans A 50 (2019) 4608–4619.

[13] J. Dennis, P.S. Bate, J.F. Humphreys, Materials Science Forum 558-559 (2007) 717–722.

[14] M. Hillert, Acta Metallurgica 13 (1965) 227–238.

[15] J. Ciulik, E.M. Taleff, Scripta Materialia 61 (2009) 895–898.

[16] M. Vollmer, Thermische Prozessierung & funktionale Charakterisierung von Fe-Mn-Al-Ni-basierten Formgedächtnislegierungen, Universität Kassel.

[17] S. Sugimoto, M. Okada, M. Homma, Journal of Applied Physics 63 (1988) 3707.

[18] S. Sugimoto, H. Satoh, M. Okada, M. Homma, Materials Transactions, JIM 32 (1991) 557–561.

[19] S. Sugimoto, H. Satoh, M. Okada, M. Homma, IEEE transactions on magnetics 27 (1991) 3412–3419.

[20] T. Omori, T. Kusama, S. Kawata, I. Ohnuma, Y. Sutou, Y. Araki, K. Ishida et al., Science (New York, N.Y.) 341 (2013) 1500–1502.

[21] T. Kusama, T. Omori, T. Saito, S. Kise, T. Tanaka, Y. Araki, R. Kainuma, Nature communications 8 (2017) 354.

[22] F.J. Humphreys, Acta Materialia 45 (1997) 4231–4240.

[23] T. Omori, H. Iwaizako, R. Kainuma, Materials & Design 101 (2016) 263–269.

[24] M. Vollmer, T. Arold, M.J. Kriegel, V. Klemm, S. Degener, J. Freudenberger, T. Niendorf, Nature communications 10 (2019) 2337.

[25] J. Xia, T. Omori, R. Kainuma, Scripta Materialia 187 (2020) 355–359.

[26] H. Ozcan, D. Salas, J. Ma, Y. Ren, Y.I. Chumlyakov, I. Karaman, Acta Materialia 242 (2023) 118465.

[27] S. Kise, A. Mohebbi, M.S. Saiidi, T. Omori, R. Kainuma, K.C. Shrestha, Y. Araki, Smart Mater. Struct. 27 (2018) 65025.

[28] F. Hosseini, B. Gencturk, A. Jain, K. Shahzada, Engineering Structures 198 (2019) 109531.

[29] M. Vollmer, A. Bauer, J.-M. Frenck, P. Krooß, A. Wetzel, B. Middendorf, E. Fehling et al., Engineering Structures 241 (2021) 112430.

[30] M. Vollmer, P. Krooß, I. Karaman, T. Niendorf, Scripta Materialia 126 (2017) 20–23.

[31] T. Omori, K. Ando, M. Okano, X. Xu, Y. Tanaka, I. Ohnuma, R. Kainuma et al., Science (New York, N.Y.) 333 (2011) 68–71.

[32] M. Vollmer, A. Bauer, M.J. Kriegel, M. Motylenko, T. Niendorf, Scripta Materialia 194 (2021) 113619.

[33] L.W. Tseng, J. Ma, B.C. Hornbuckle, I. Karaman, G.B. Thompson, Z.P. Luo, Y.I. Chumlyakov, Acta Materialia 97 (2015) 234–244.

[34] H. Ozcan, J. Ma, I. Karaman, Y.I. Chumlyakov, R. Santamarta, J. Brown, R.D. Noebe, Scripta Materialia 142 (2018) 153–157.

[35] T. Omori, M. Nagasako, M. Okano, K. Endo, R. Kainuma, Appl. Phys. Lett. 101 (2012) 231907.

[36] A. Walnsch, M.J. Kriegel, O. Fabrichnaya, A. Leineweber, Calphad 66 (2019) 101621.

[37] N. Schell, A. King, F. Beckmann, T. Fischer, M. Müller, A. Schreyer, Materials Science Forum 772 (2013) 57–61.

[38] S. Lin, U. Borggren, A. Stark, A. Borgenstam, W. Mu, P. Hedström, Metall and Mat Trans A 52 (2021) 1812–1825.

[39] G. Ashiotis, A. Deschildre, Z. Nawaz, J.P. Wright, D. Karkoulis, F.E. Picca, J. Kieffer, J Appl Crystallogr 48 (2015) 510–519.

[40] J. Kieffer, G. Ashiotis, PyFAI: a Python library for high performance azimuthal integration on GPU, 2014.

[41] F. Bachmann, R. Hielscher, H. Schaeben, SSP 160 (2010) 63–68.

[42] H.-R. Wenk, S. Grigull, J Appl Crystallogr 36 (2003) 1040–1049.

[43] P. Virtanen, R. Gommers, T.E. Oliphant, M. Haberland, T. Reddy, D. Cournapeau, E. Burovski et al., Nature methods 17 (2020) 261–272.

[44] A.P. Day, T.E. Quested, Journal of microscopy 195 (1999) 186–196.

[45] M. Ermrich, D. Opper, XRD for the analyst: Getting acquainted with the principles, 2nd ed., PANalytical, Almelo, 2013.

[46] M. Kutsal, P. Bernard, G. Berruyer, P.K. Cook, R. Hino, A.C. Jakobsen, W. Ludwig et al., IOP Conf. Ser.: Mater. Sci. Eng. 580 (2019) 12007.

[47] L. Spieß, G. Teichert, R. Schwarzer, H. Behnken, C. Genzel, Moderne Röntgenbeugung, Springer Fachmedien Wiesbaden, Wiesbaden, 2019.

[48] H. Simons, A. King, W. Ludwig, C. Detlefs, W. Pantleon, S. Schmidt, I. Snigireva et al., Nature communications 6 (2015) 6098.

[49] A.P. Sutton, R.W. Balluffi, Interfaces in Crystalline Materials, OUP Oxford, 2006.

[50] P. Lejcek, Grain Boundary Segregation in Metals, Springer Berlin Heidelberg, Berlin, Heidelberg, 2010.

[51] J.C.M. Li, J. Appl. Phys. 33 (1962) 2958–2965.

[52] S. Xu, T. Kusama, X. Xu, H. Huang, T. Omori, J. Xie, R. Kainuma, Materialia 6 (2019) 100336.

[53] R. Sandström, B. Lehtinen, E. Hedman, I. Groza, S. Karlsson, J Mater Sci 13 (1978) 1229–1242.

Figure1

Click here to access/download;Figure(s);figure1.jpg

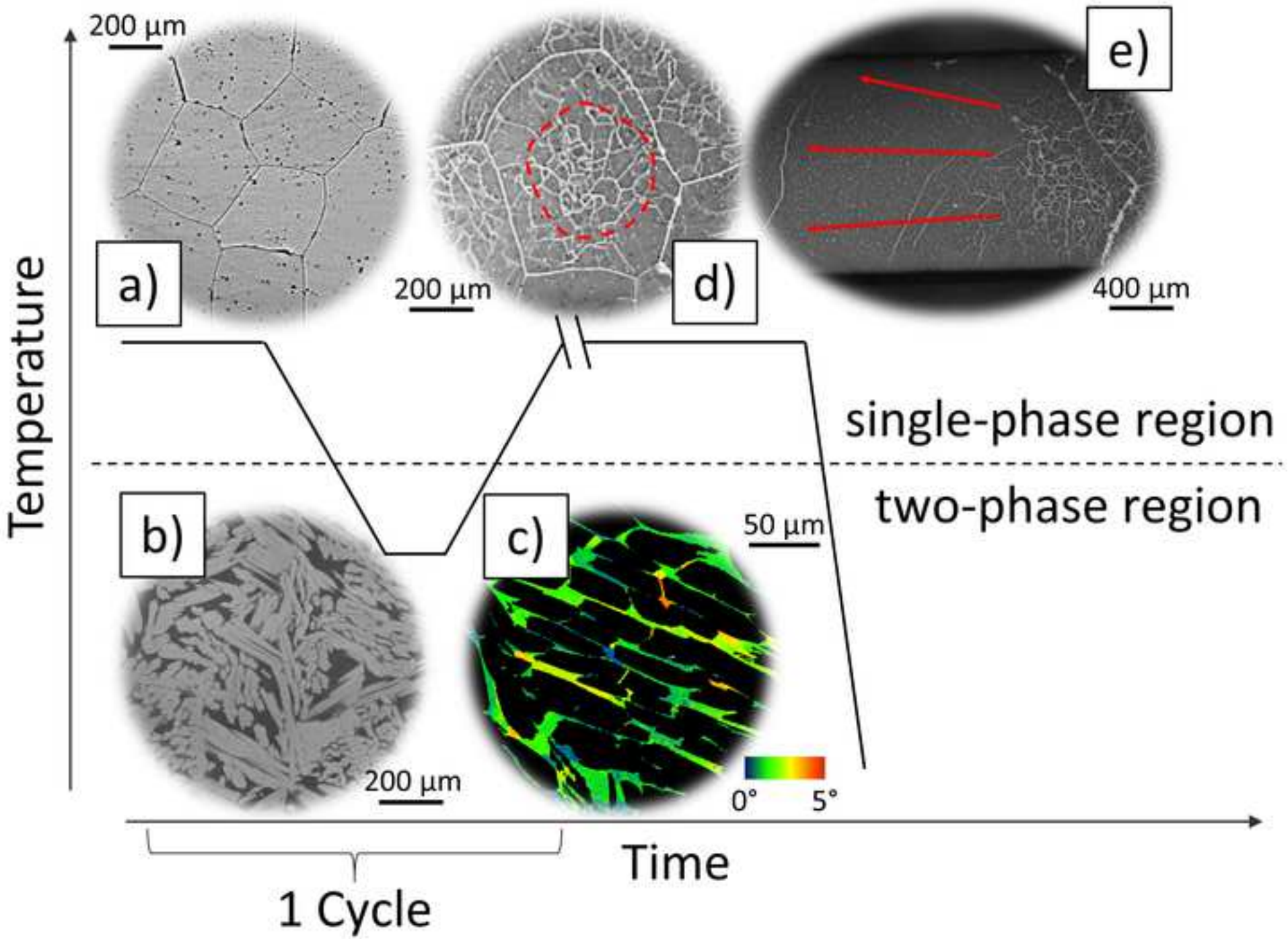

Figure2

Click here to access/download;Figure(s);figure2.jpg

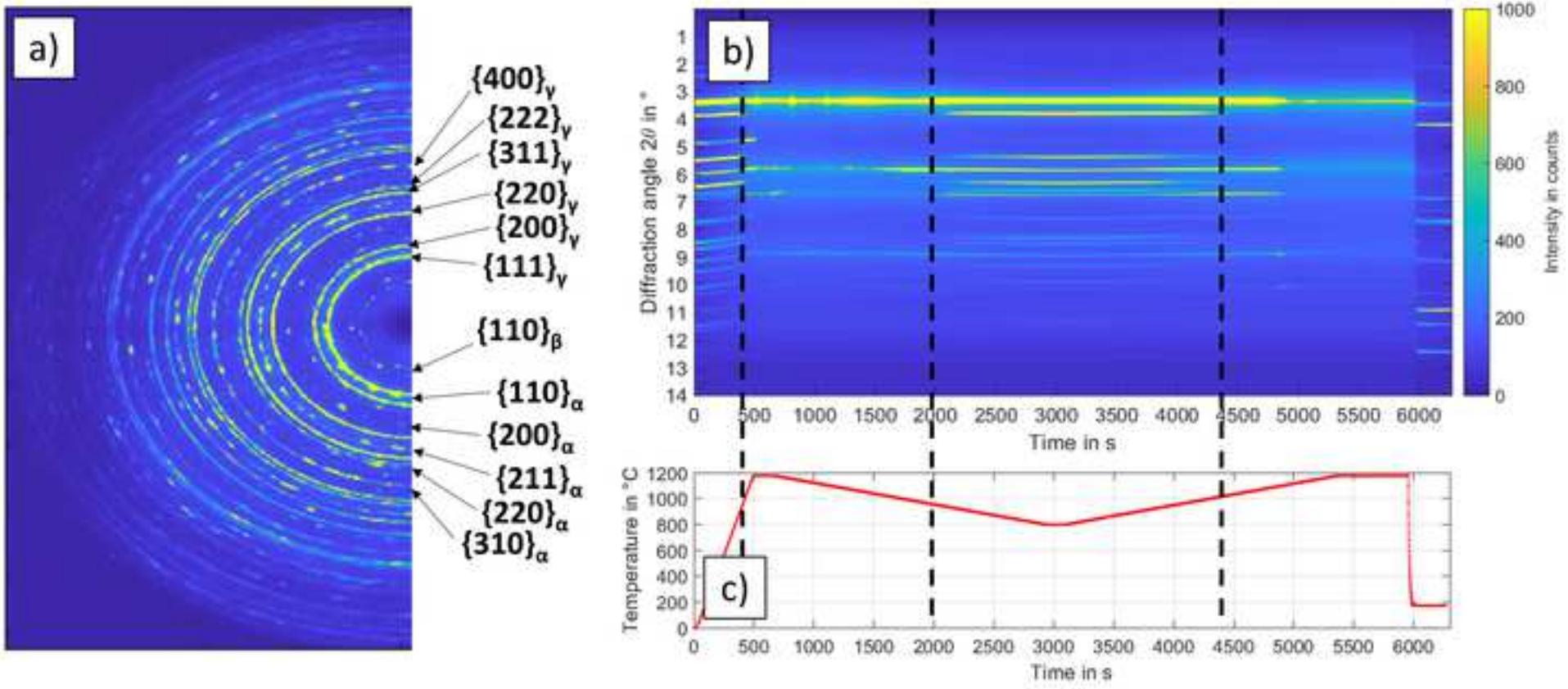

Figure3

Click here to access/download;Figure(s);figure3.jpg

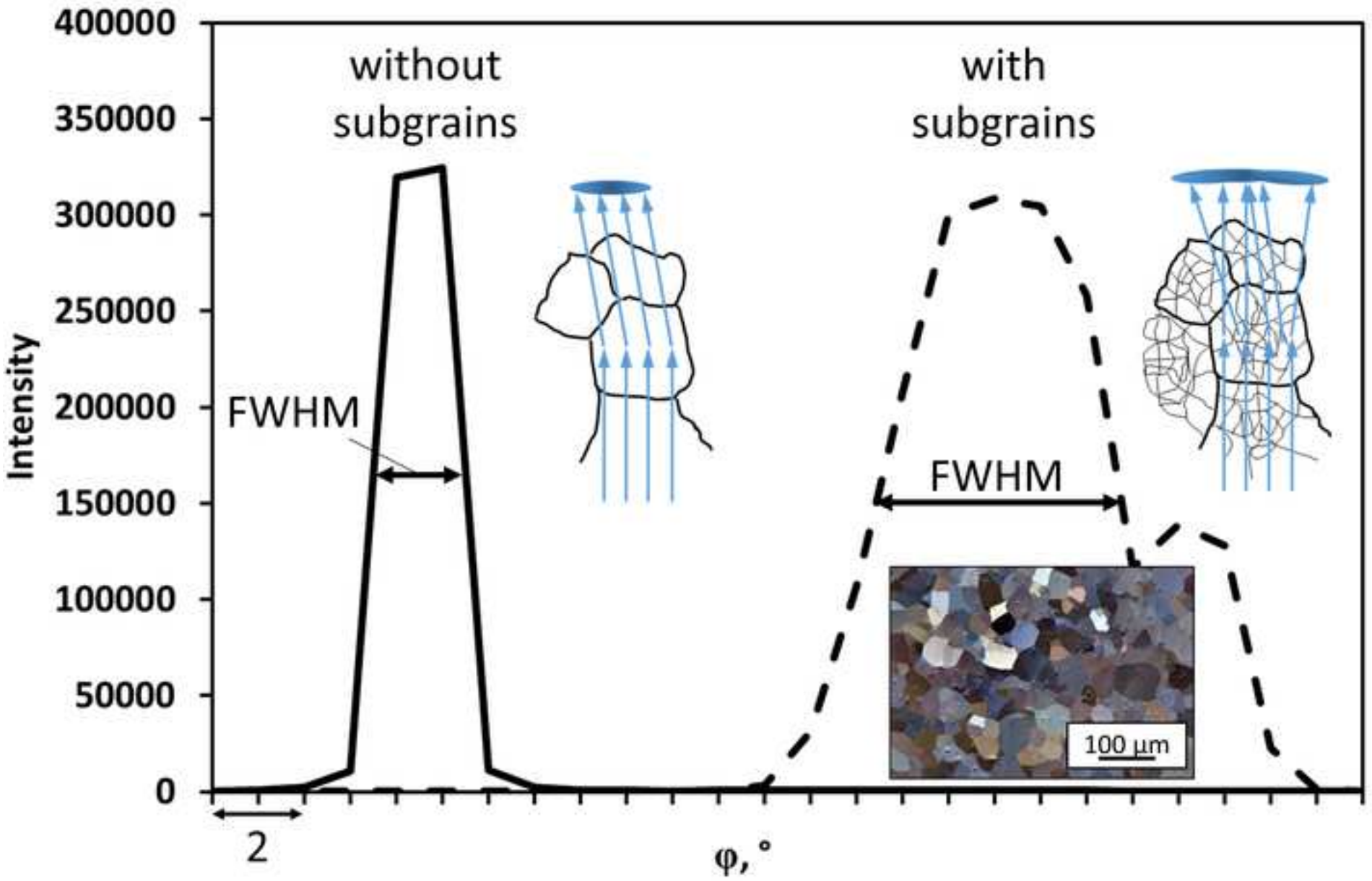

Figure4

Click here to access/download;Figure(s);figure4.jpg

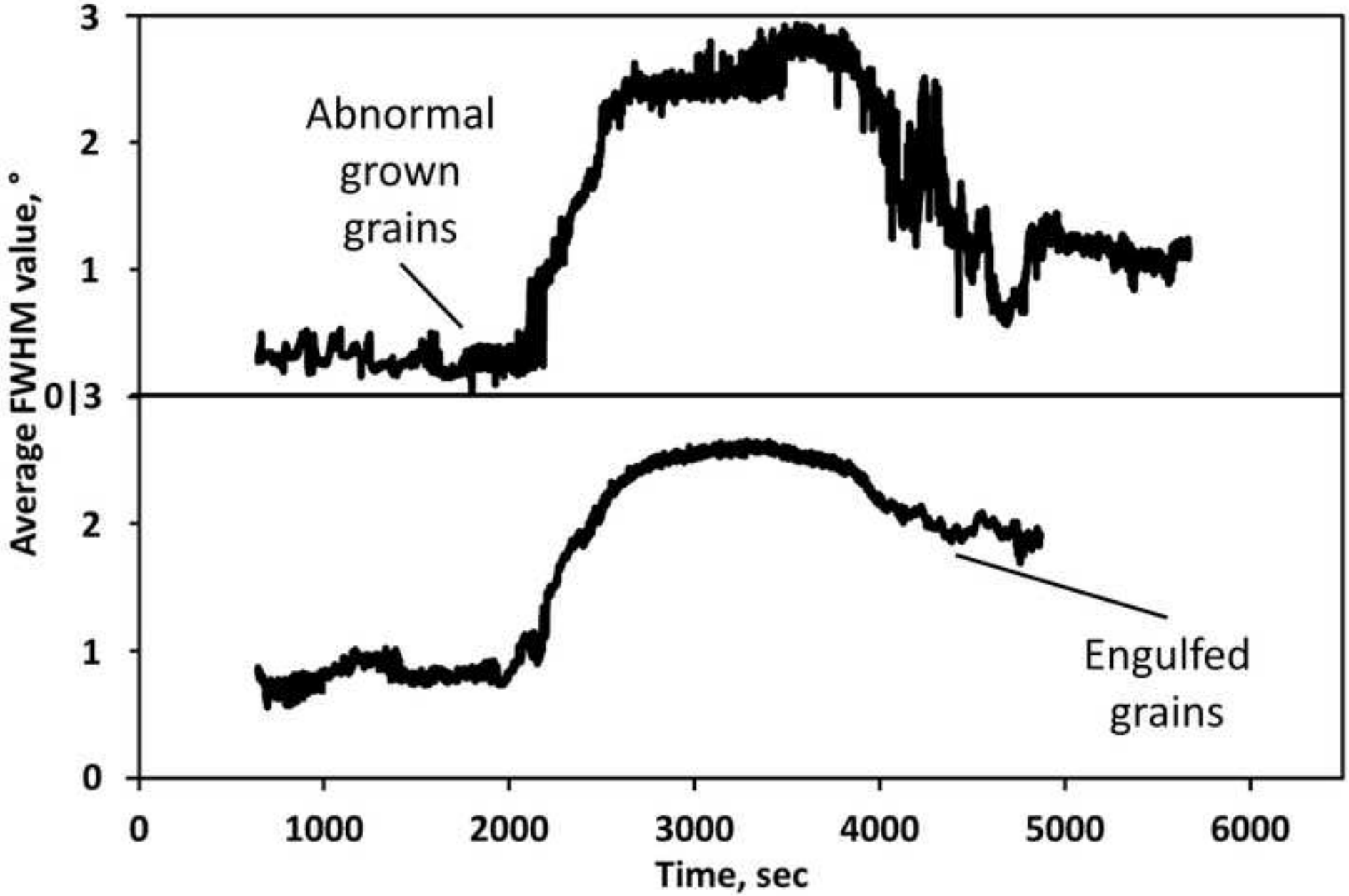

Figure5

Click here to access/download;Figure(s);figure5.jpg

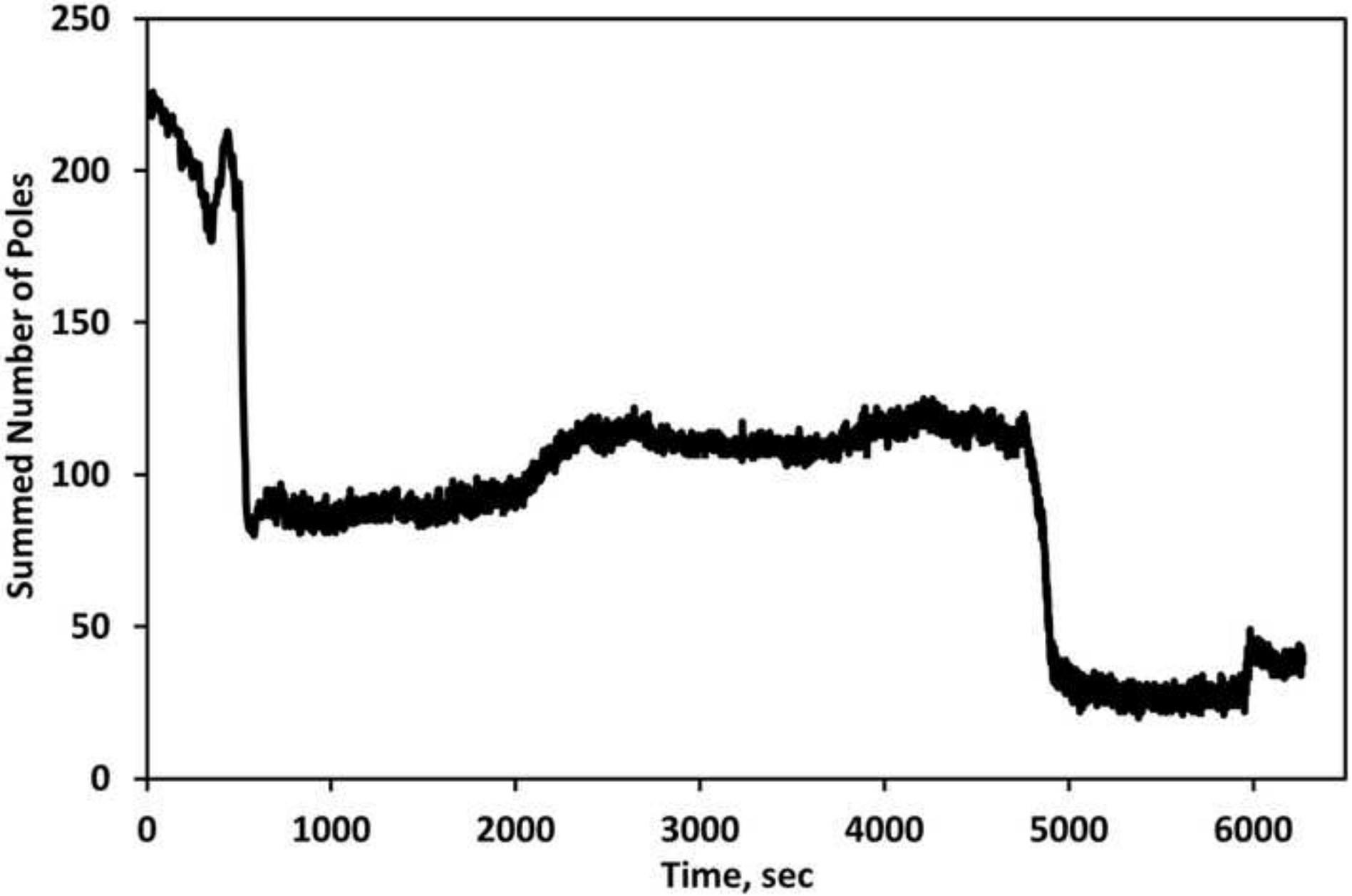

Figure6

Click here to access/download;Figure(s);figure6.jpg

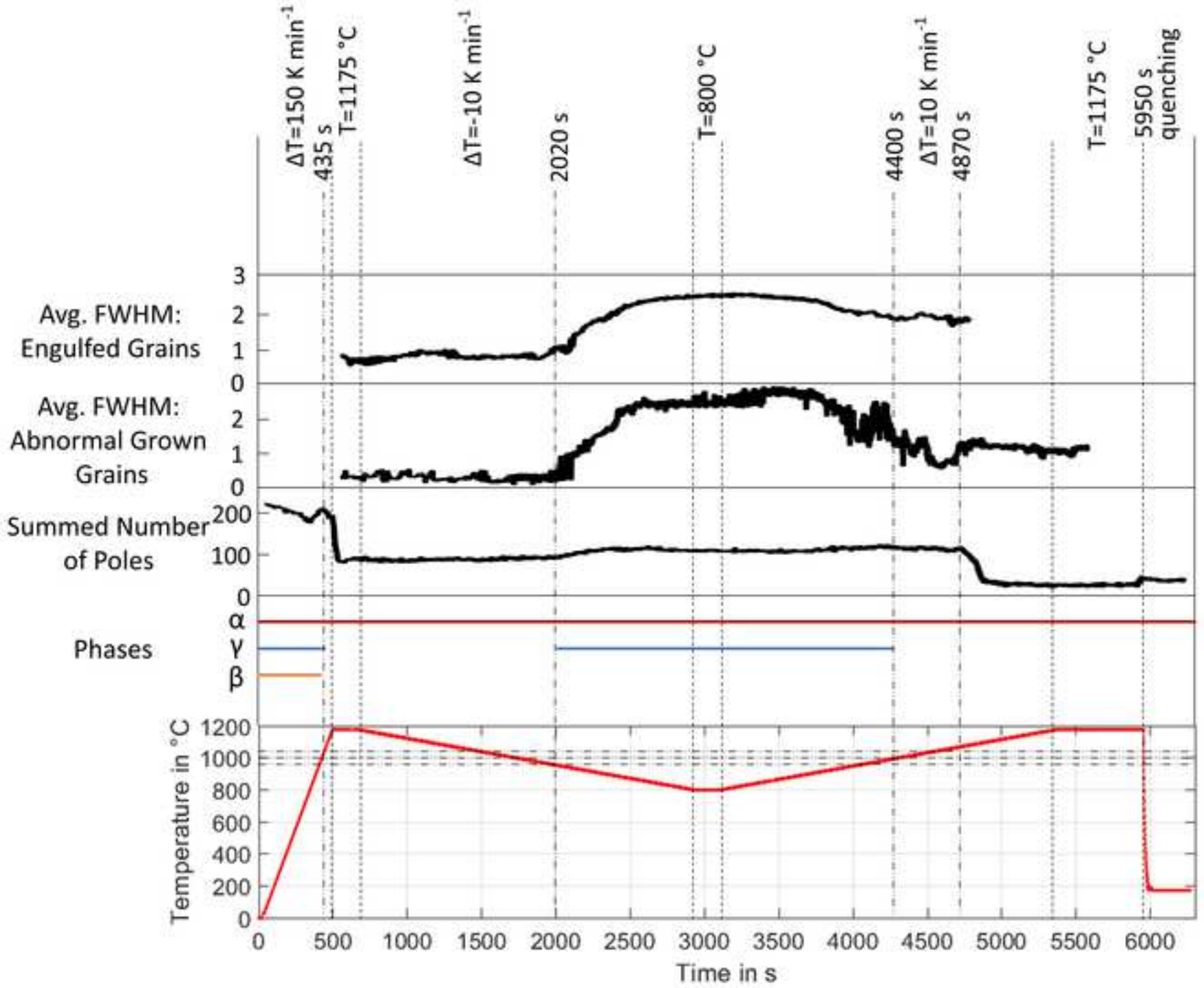

Figure7

Click here to access/download;Figure(s);figure7.jpg

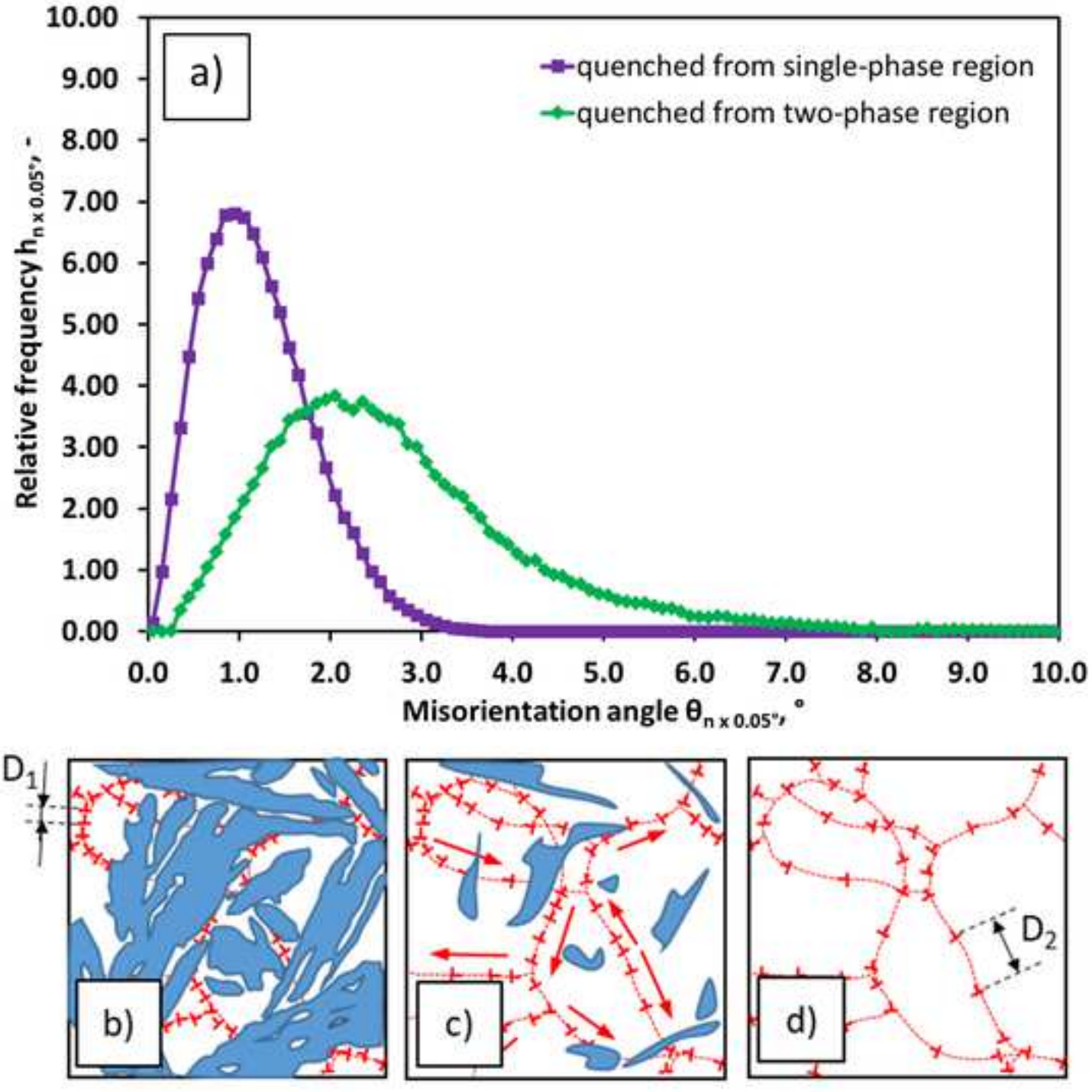

Click here to access/download;Figure(s);figure8.jpg

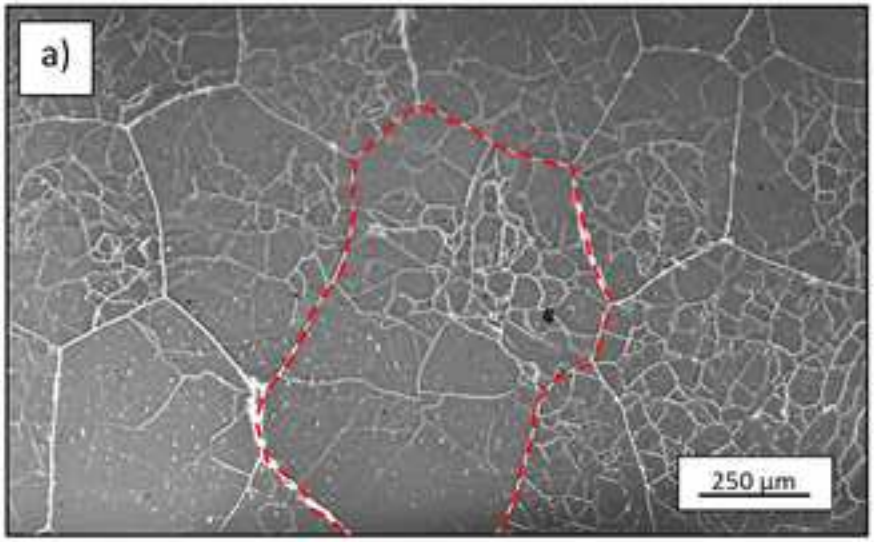

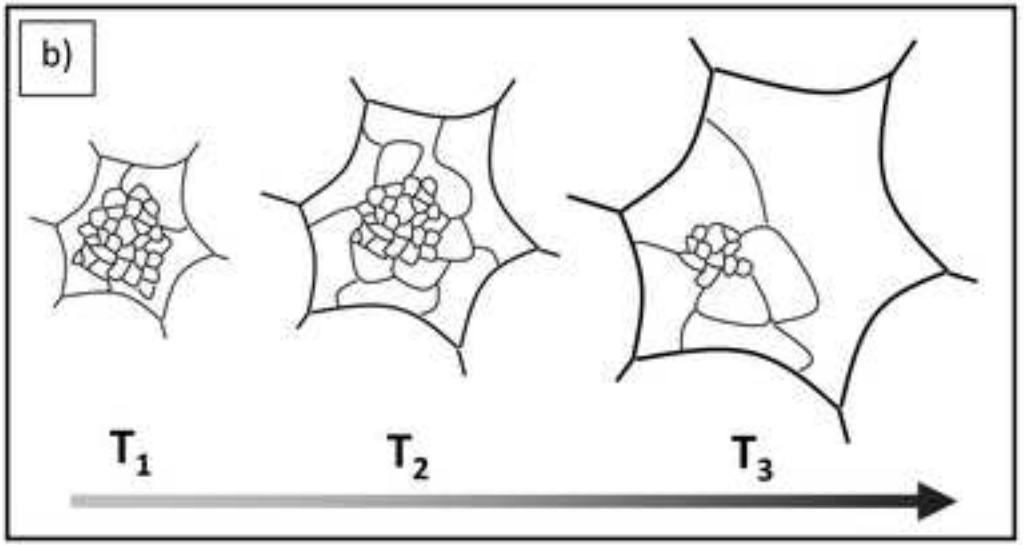

Figure9

Click here to access/download;Figure(s);figure9.jpg

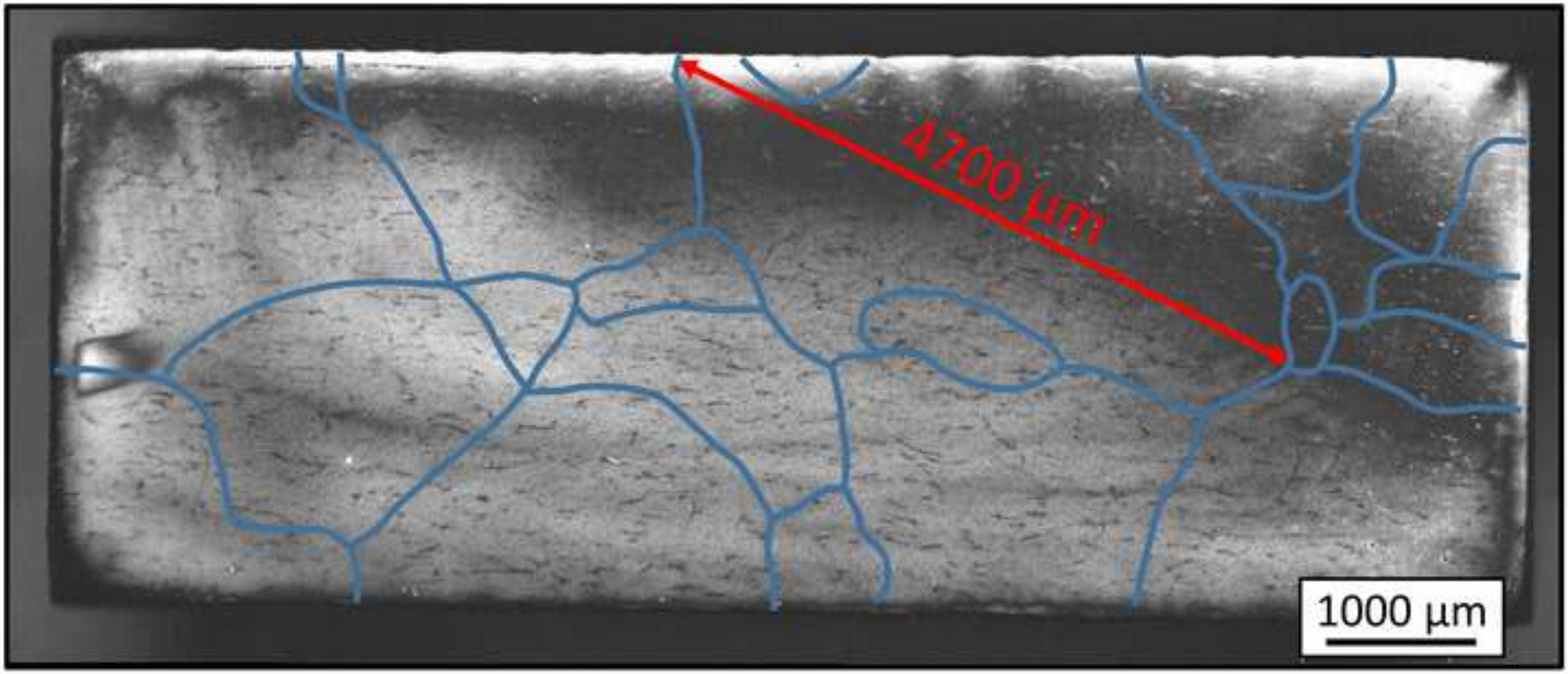

Table1

Click here to access/download;Table(s);tab1.jpg

Specimen	Alloy	Heat treatment	Investigations				
			in situ HEXRD	ex situ HEXRD	OM	EBSD	COCI
1	Fe-Mn-Al-Ni-Ti	A	x		x	x	
2	Fe-Mn-Al-Ni-Ti	B		x			x
3	Fe-Mn-Al-Ni-Ti	C		x			x
4	Fe-Mn-Al-Ni-Ti	C				x	
5	Fe-Mn-Al-Ni-Ti	D				x	
6	Fe-Mn-Al-Ni	E			x		

A: 2.5 K min^{-1} --> 1175°C 3 min --> 10 K min^{-1} --> 800°C 3 min --> 10 K min^{-1} --> 1175°C 10 min --> quenched

B: 1225°C 60 min --> water quenched

C: 1225°C 30 min --> 10 K min^{-1} --> 900°C 15 min ---> 10 K min^{-1} --> 1050°C 0 min --> water quenched

D: 1225°C 30 min --> 10 K min^{-1} --> 900°C 15 min --> water quenched

E: 1225°C 30 min --> 10 K min^{-1} --> 900°C 15 min ---> 10 K min^{-1} --> 1225°C 0 min --> water quenched

Graphical Abstract

Time resolved insights into abnormal grain growth:

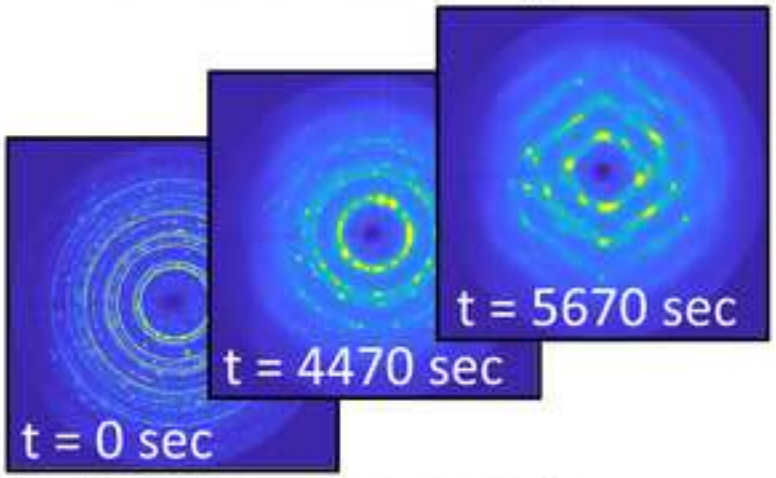

In Situ Synchrotron High Energy X-Ray Diffraction

Microstructural Characterisation

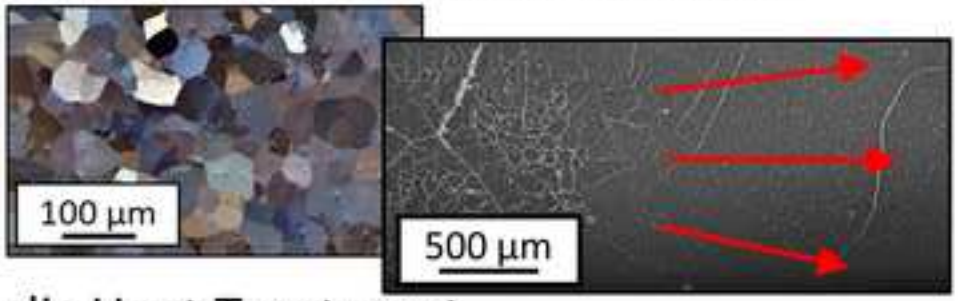
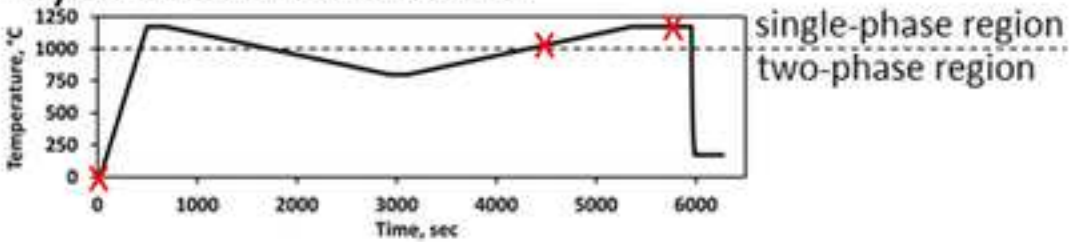
Cyclic Heat Treatment